nature communications

Article

https://doi.org/10.1038/s41467-024-55556-5

A stable open-shell *peri*-hexacene with remarkable diradical character

Received: 22 August 2024

Accepted: 16 December 2024

Published online: 02 January 2025

Check for updates

Jinji Zhang[1,7], Xiaojing Fang[1,7], Weiwei Niu[2,7], Yiming Yu[1], Yanlin Hu[1], Jiawen Sun[1], Ying Xu[1], Zhihua Zhou[3], Heyuan Liu[4], Xiaonan Fan[4], Baishu Zheng[3] ✉, Qing Jiang[5] ✉, Guangwu Li[2,6] ✉ & Wangdong Zeng[1] ✉

[n]*Peri*-acenes ([n]PA) have attracted great interest as promising candidates for nanoelectronics and spintronics. However, the synthesis of large [n]PA ($n > 4$) is extremely challenging due to their intrinsic open-shell radical character and high reactivity. Herein, we report the successful synthesis and isolation of a derivative (1) of *peri*-hexacene in crystalline form. The structure of 1 is unequivocally confirmed by X-ray crystallographic analysis. Its ground state, aromaticity and photophysical properties are systematically studied by both experimental methods and theoretical calculations. Although the parent *peri*-hexacene is calculated to have a very large diradical character ($y_0 = 94.5\%$), 1 shows reasonable stability ($t_{1/2} = 24$ h under ambient conditions) due to the kinetic blocking. 1 exhibits an open-shell singlet ground state with a small singlet-triplet energy gap (−1.33 kcal/mol from SQUID measurements). 1 has also a narrow HOMO-LUMO energy gap (1.05 eV) and displays amphoteric redox behavior. This work opens new avenues for the design and synthesis of stable zigzag-edged graphene-like molecules with significant diradical character.

Atomically precise nanographenes (NGs) have gained intensive attention in the past decade because of their fascinating optoelectronic properties and high promise for next-generation semiconductor materials[1–10]. Both experimental and computational studies have demonstrated that widths and edge topologies of NGs play a pivotal role in determining their electronic and magnetic properties as well as their chemical reactivities[11–13]. Among various NG families, [n]*peri*-acenes ([n]PAs), where n defines the number of benzene rings formed along the zigzag axis, are a unique class of rectangle-shaped NGs consisting of two zigzag-edges and two arm-chair-edges, which can exhibit, if n exceeds a certain threshold ($n > 3$), diradical and even polyradical character upon the lateral π-extension due to the gain of additional Clar's aromatic sextets in their open-shell resonance forms (Fig. 1)[14–21]. They can also be considered as ideal model molecules to explore the electronic structures of the large-size NGs with zigzag edges[22–24]. However, their synthesis is a huge challenge owing to their intrinsic open-shell radical character, which is related to the presence of a localized non-bonding π-state around parallel zigzag edges. To date, only a few [n]PA molecules have been successfully synthesized. For example, in 2018, Feng and Wu's groups independently reported the in-solution synthesis of *peri*-tetracene derivatives ([4]PA, Fig. 1a), showing large diradical character with a half-life of 3–7 h in solution

[1]School of Materials Science and Engineering, Hunan University of Science and Technology, Xiangtan, China. [2]Center of Single-Molecule Sciences, Institute of Modern Optics, Tianjin Key Laboratory of Micro-Scale Optical Information Science and Technology, College of Electronic Information and Optical Engineering, Nankai University, Tianjin, China. [3]Key Laboratory of Theoretical Organic Chemistry and Function Molecule of Ministry of Education, Hunan Provincial Key Laboratory of Controllable Preparation and Functional Application of Fine Polymers, School of Chemistry and Chemical Engineering, Hunan University of Science and Technology, Xiangtan, China. [4]School of Materials Science and Engineering, China University of Petroleum (East China), Qingdao, Shandong, China. [5]College of Chemistry and Bioengineering, Hunan University of Science and Engineering, Yongzhou, China. [6]Shenzhen Research Institute of Nankai University, Shenzhen, China. [7]These authors contributed equally: Jinji Zhang, Xiaojing Fang, Weiwei Niu. ✉e-mail: zbaishu@163.com; qjiang198@163.com; ligw@nankai.edu.cn; wangdong.zeng@hnust.edu.cn

https://doi.org/10.1038/s41467-024-55556-5

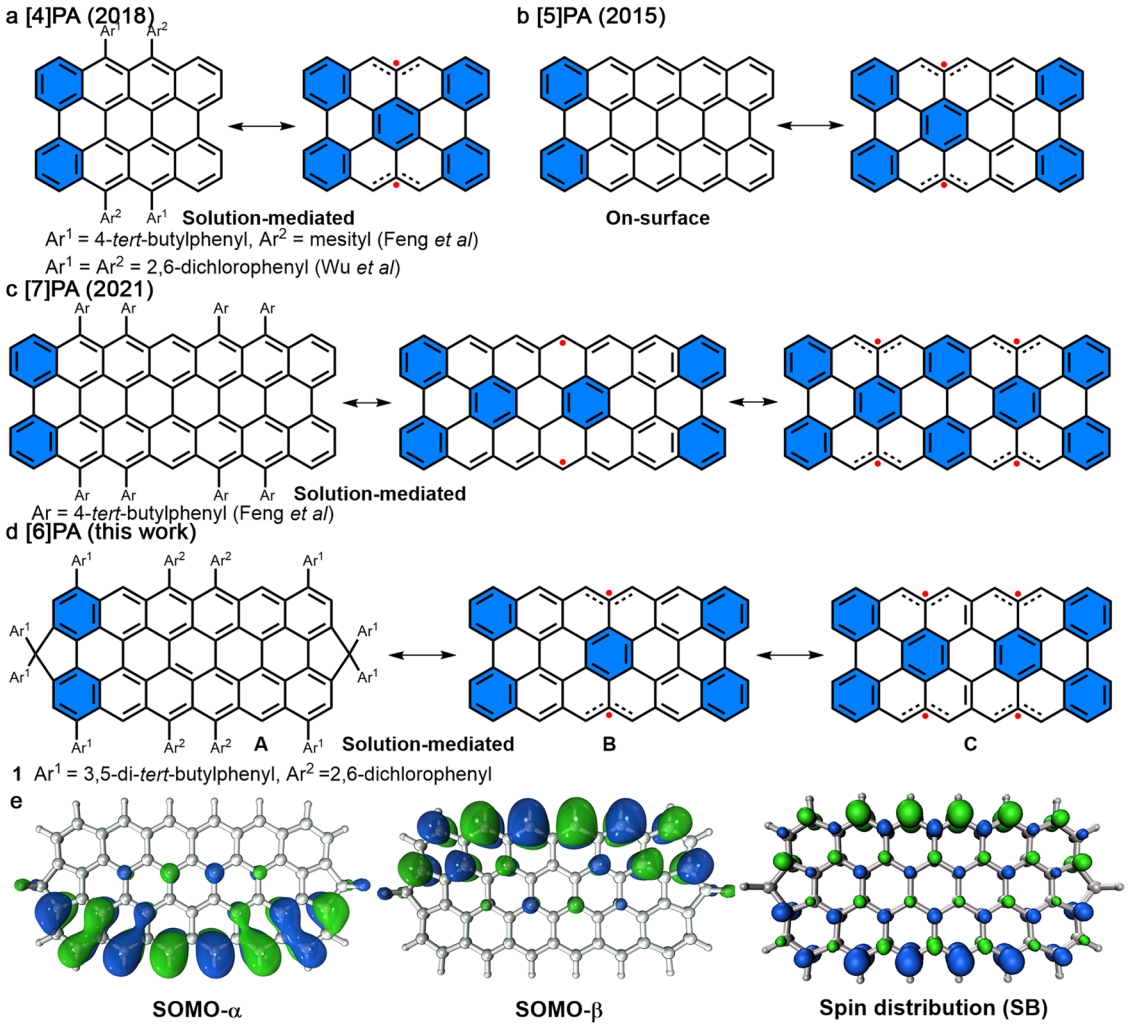

Fig. 1 | Representative closed-shell and open-shell diradical resonance forms of *peri*-acenes. a [4]PA derivatives; **b** parent [5]PA; **c** [7]PA derivative, and **d** the new [6]PA derivative. The substituents in [4]PA, [7]PA and [6]PA are omitted in the open-shell resonance structures for clarity. The rings shaded in blue denote aromatic sextets. **e** Calculated (UB3LYP/6-31G(d,p)) SOMO-α, SOMO-β and spin density distribution map of singlet biradical (SB) form of parent [6]PA.

under ambient conditions[25,26]. In 2021, Feng's group described the in-solution synthesis and in-situ characterization of hitherto the largest *peri*-heptacene derivative ([7]PA, Fig. 1c), which demonstrated a significant tetraradical character with a half-life of ~25 min under inert conditions[27]. It should be mentioned that parent *peri*-pentacene ([5]PA, Fig. 1b) has been accomplished on Au (III) surface under ultra-high vacuum conditions and its singlet open-shell nature was revealed by scanning tunneling spectroscopy[28], but all attempts so far to synthesize [5]PA or its derivatives in solution have been unsuccessful due to the poor solubility and undesired side reactions[29,30]. Therefore, the solution-phase synthesis of large [n]PAs ($n > 4$) or their appropriate derivatives depends heavily on the development of more effective design and synthetic strategies, which need to overcome the challenges associated with the low solubility and the intrinsic high reactivity of the target molecules.

Peri-hexacene ([6]PA, Fig. 1d), which has been achieved difficultly by solution-mediated or surface-assisted synthesis, is the next important target of synthesis and isolation, and its realization is also crucial for elucidating the structure-property relationship of this family from both fundamental and applied perspectives. In this context, herein we report the solution-phase synthesis and characterization of a stable *peri*-hexacene derivative (**1**, Fig. 1d). To obtain preliminary insights into the stability and properties of **1**, Clar's aromatic π-sextet rule was utilized. The Clar's rule is a fundamental concept in the chemistry of polycyclic aromatic hydrocarbons (PAHs) and posits that the Kekulé resonance structure with the highest number of disjoint benzene-like aromatic π-sextets—referred to as "Clar's sextets"—has the most contribution to the properties of the PAH. Generally, an isomeric PAH with more Clar's sextets is expected to exhibit higher stability[14–16]. Recent studies have highlighted the importance of additional aromatic sextet rings on stabilizing the diradical structure[25–28,31–38]. Specifically, the gain of one or more additional Clar's sextets in the open-shell form is crucial for achieving a stable ground-state singlet diradicaloid with high diradical character. According to this rule, the molecule can be drawn in at least three different resonance forms: a closed-shell form with two aromatic sextet rings (the hexagons shaded in blue, form A), an open-shell diradical form with five aromatic sextet rings (form B), and an open-shell tetraradical form with six aromatic sextet rings (form C). The gain of three/four Clar's aromatic sextet rings in the open-shell resonance forms B/C implies a large diradical character and moderate tetraradical character. Our spin-unrestricted theoretical calculations (UB3LYP/6-31 G(d,p) on the parent [6]PA indicated that the frontier SOMO-α and SOMO-β orbitals have significant disjoint features, and the high spin densities are mainly distributed along the two zigzag edges (Fig. 1e). Thus, the diradical character (y_0) and tetraradical character (y_1) of the parent [6]PA were calculated to be 94.5% and 24.5%, respectively, by the Natural orbital occupation number (NOON) calculations (UCAM-B3LYP/6-31G(d,p))[39], which is much larger than [4]

https://doi.org/10.1038/s41467-024-55556-5

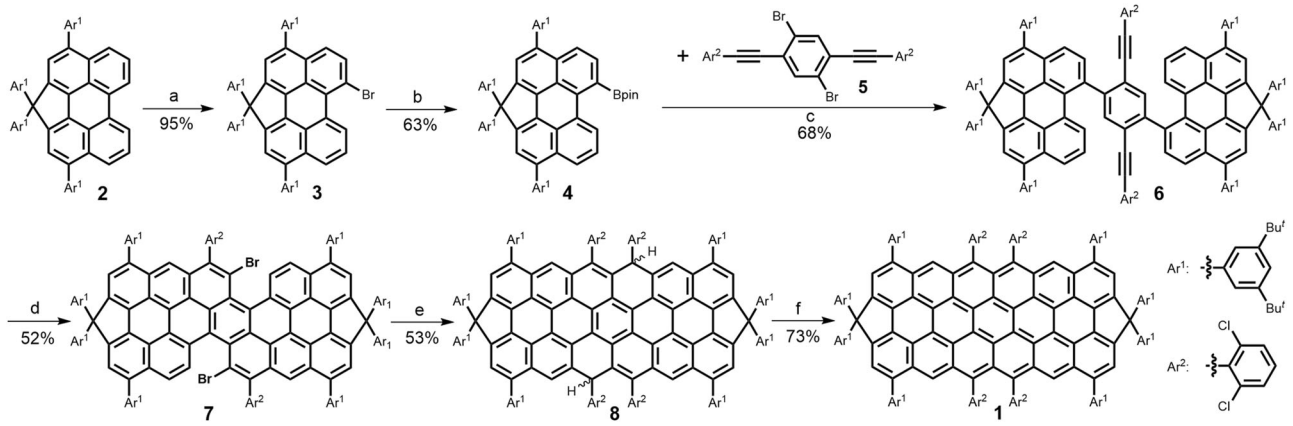

Fig. 2 | Synthetic route toward *peri*-hexacene derivative 1. a Br_2, DCM, 0 °C, 30 min; **b** $Pd(dppf)Cl_2$, $B_2(pin)_2$, KOAc, dioxane, 90 °C; **c** $Pd(PPh_3)_4$, SPhos, K_3PO_4, toluene/H_2O, 90 °C; **d** $CuBr_2$, K_3PO_4, DCE, reflux; **e** i) *n*-BuLi, −30 °C; ii) 2,6-dichlorobenzaldehyde, rt; iii) TfOH, DCM, rt; **f** i) $KOBu^t$, 18-crown-6, THF, rt; ii) *p*-chloranil. SPhos: 2-Dicyclohexylphosphino-2′,6′-dimethoxybiphenyl; DCE: 1,2-dichloroethane; THF: tetrahydrofuran; DCM: dichloromethane.

PA (y_0 = 52.5%) and [5]PA (y_0 = 75.4%) under the same level of theory. The significant open-shell radical character of [6]PA suggests the need to kinetically block the most reactive zigzag edges by bulky groups and to develop an innovative strategy to build up the framework. In response to these challenges, a soluble and stable [6]PA derivative **1** was successfully synthesized and isolated in a crystalline form. Its ground state, aromaticity and photophysical properties were systematically explored by both experimental methods and theoretic calculations and compared with those of [4]PA and [7]PA derivatives.

Results

To realize the synthesis of [6]PA with sufficient stability and solubility, our strategy is to introduce four bulky and electron-withdrawing 2,6-dichlorophenyl groups at the most reactive sites of the two zigzag edges and to incorporate C(sp^3)-bridged cyclopenta (CP) rings at the bay regions of [6]PA where each sp^3 carbon substituted by two 3,5-di-*tert*-butylphenyl groups. The incorporation of CP rings in these bay regions not only enhances solubility but also restrain the Diels-Alder reaction in these areas, a phenomenon observed in the previous report concerning the synthesis of peri-tetracene derivative[25]. In addition to these substituents, four additional 3,5-di-*tert*-butylphenyl groups are also attached onto the π-conjugated framework to further improve solubility. As depicted in Fig. 2, the key intermediate for the synthesis of the target molecule **1** is the partially fused dibromo-intermediate **7**, which is prepared via multiple cross-coupling, regioselective cyclization and oxidative dehydrogenation reactions. The CP ring-fused perylene **2** was synthesized from parent perylene according to our reported procedure[40,41]. The monobromo CP-fused perylene **3** was firstly synthesized by regio-selective bromination with bromine under controlled conditions at the bay region, and then Miyaura borylation reaction of **3** with bis(pinacolato)diboron ($B_2(pin)_2$)in the presence of palladium catalyst provided monoboronic ester **4** in 63% yield. After that, the Suzuki coupling of **5** with **4** yielded the intermediate **6** in 68% yield. Next, the key intermediate **7** was obtained by the treatment of **6** with $CuBr_2$ in the presence of base where a one-pot reaction of benzannulation and intramolecular oxidative cyclodehydrogenation was achieved. This method differs from the stepwise syntheses typically reported for *peri*-acene derivatives[25–27]. Our one-pot strategy not only streamlines the procedure but also enhances overall efficiency, thereby providing an alternative pathway for the construction of other graphene fragments. The structure of **7** was confirmed by single-crystal analysis (Supplementary Fig. 22). Afterwards, lithium-halogen exchange reaction by treatment of **7** with *n*-BuLi proceeds and subsequent quenching with 2,6-dichlorobenzaldehyde to generate the diol, which underwent an intramolecular Friedel-Crafts cyclization in the presence of trifluoromethanesulfonic acid (TfOH) to afford the dihydro- precursor **8** in 53% yield over three steps from **7**. Finally, the deprotonation of 8 with ^{t}BuOK and 18-crown-6 in THF followed by the oxidation with *p*-chloranil furnished the target *peri*-hexacene derivative **1** in 73 % yield. Because two cyclopenta (CP) ring was attached onto the arm-chair edges and the four bulky and electron-withdrawing 2,6-dichlorophenyl groups are attached onto the most reactive zig-zag edges, compound **1** shows good solubility and stability, and can be purified by triethylamine deactivated silica gel column. Stability test of the solution of **1** in carbon tetrachloride under ambient air and light conditions followed by UV/Vis-NIR absorption measurements revealed a half-life time ($t_{1/2}$) of about 24 h when monitored at 617 nm (Supplementary Fig. 1). During the submission of our work, Wu et al. reported the synthesis of both *peri*-pentacene and *peri*-hexacene derivatives utilizing a similar synthetic strategy[42]. Their studies indicated that the *peri*-hexacene derivative exhibited remarkable stability, with its absorbance at the maximum decreasing by only 1% after 72 hours of exposure to ambient air and light, which surpassed the stability of our *peri*-hexacene derivative **1** under similar conditions. The exceptional stabilities observed in their work can be ascribed to the protection of the zigzag edges with bulky groups through a synergistic captodative effect, wherein the electron donor and acceptor collaboratively stabilize the radicals by forming a zwitterionic radical structure. In contrast to the stabilization strategy based on kinetic blocking combined with a synergistic captodative effect, our design employed kinetic protection of both zigzag edges and bay regions by bulky groups with similar electronic characteristics, resulting in reasonable stability. These findings offer valuable insights for the synthesis of a broader range of graphene fragments with zigzag edges in the future.

Single crystals of **1** suitable for X-ray crystallographic analysis were grown by slow diffusion of acetonitrile into its solution in toluene. The molecule has a centrosymmetric geometry with a slightly distorted skeleton (Fig. 3a, b). The dihedral angles between the π-conjugated skeleton and its 2,6-dichlorophenyl substituents range from 83.1 to 84.5° (Fig. 3a). Bond length analysis of the **1** backbone revealed that the bond lengths of the CC bonds (the bonds shown in red, Fig. 3c) linking the two hexacene units were in the range of 1.409-1.429 Å, which are shorter than that in [4]PA derivative (1.442–1.459 Å)[26], indicating enhanced electronic coupling between two hexacene units. The CC bonds shown in blue (Fig. 3c) are much longer (1.464 Å) like a typical C(sp^2)-C(sp^2) single bond, which could be attributed to the elongation induced by the steric hindrance between the neighboring 2,6-dichlorophenyl substituenets. The calculated harmonic oscillator model of aromaticity (HOMA) values[43] based on

https://doi.org/10.1038/s41467-024-55556-5

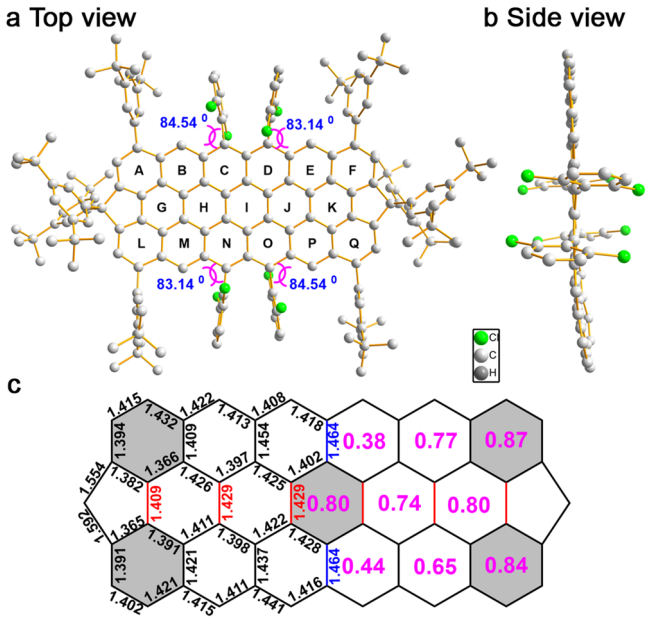

Fig. 3 | X-ray crystallographic analyses of 1. a Top view and **b** side view of **1**. **c** The selected bond lengths (in Å) of the backbone. The pink numbers in hexagons are the calculated HOMA values; the hexagons shaded in gray with large HOMA values indicate the aromatic sextet rings.

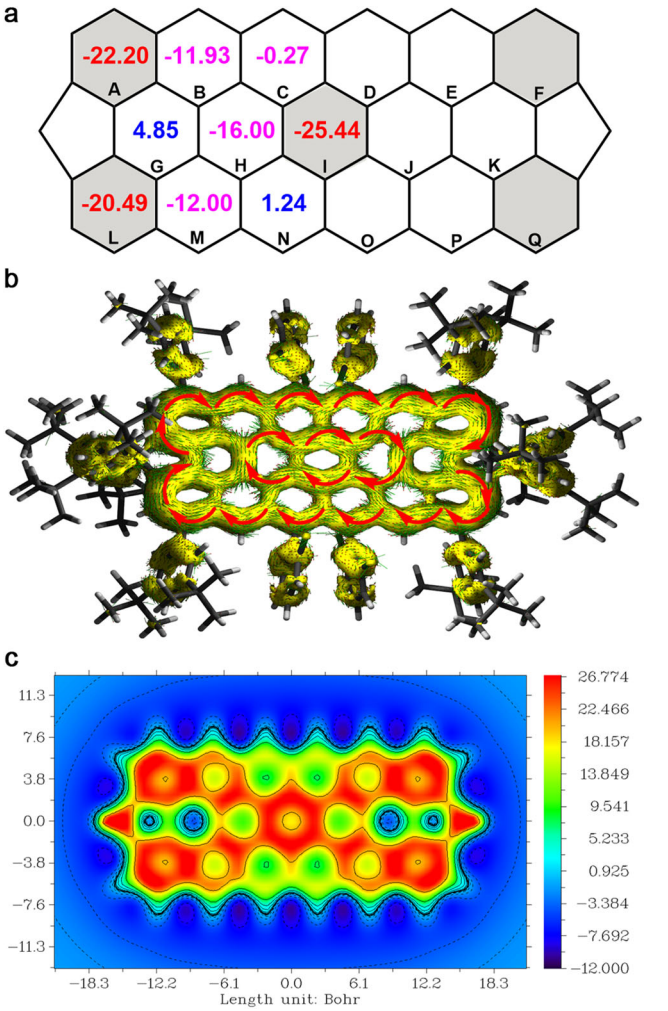

Fig. 4 | Aromatic properties of 1. a Calculated NICS(1)zz values (the numbers in the rings) of **1**. **b** Calculated ACID plot of **1** (isovalue: 0.02). The magnetic field is perpendicular to the XY plane and point out through the paper. **c** Calculated 2D ICSS map of parent peri-hexacene at 1 Å above the XY plane.

the X-ray structures revealed that the four benzenoid rings at the termini (rings A/F/L/Q) have largest HOMA values (0.87/0.84, Fig. 3c), indicating a large aromatic character. The rings C/D/N/O have much smaller HOMA values (0.38 ~ 0.44, Fig. 3c) while the other benzenoid rings have a HOMA value of 0.65–0.80 (Fig. 3c), indicating significant contribution of the open-shell diradical form B with five localized aromatic sextet rings shown in Fig. 1d to the ground-state structure. On the other hand, nucleus independent chemical shift (NICS)[44] calculations show that these five benzenoid rings have large negative NICS(1)$_{zz}$ values (−20.49 ppm to −22.20 ppm), the rings B/E/H/J/M/P have moderate negative NICS(1)$_{zz}$ values (−11.93 ppm to −16.00 ppm) while the rings C/D/N/O are almost non-aromatic (Fig. 4a). All these suggest that [6]PA possesses a large diradical character, which can be stabilized by five aromatic sextet rings. In addition, no intermolecular π-π interaction was observed in the 3D packing structure (Supplementary Fig. 23).

To gain a deeper understanding of the electronic structure and aromaticity of compound **1**, we carried out anisotropy of induced current-density (ACID)[45] and isochemical shielding surface (ICSS)[46,47] calculations (B3LYP/6-31 G(d,p)). ACID plot shows obvious clockwise diatropic ring current circuit along the periphery (Fig. 4b), indicating that the molecule is globally aromatic and the two hexacene units are coupled well with each other, in accordance with the bond length analysis. Notably, the central anthracene units show clockwise diatropic ring current (Fig. 4b), in agreement with the HOMA value and NICS analysis. Furthermore, the calculated 2D ICSS map also shows that the rings A/F/L/Q have the strongest shielding, the rings B/E/H/J/M/P have moderate shielding, and there is the least shielding in other benzenoid rings (Fig. 4c), consistent with the NICS and ACID calculations. For comparison, although the open-shell diradical form of [4]PA exhibits a localized aromatic character (Fig. 1a), the central benzenoid ring connecting the two tetracene units in[4]PA is almost non-aromatic[26]. The central benzenoid rings connecting the two hexacene/heptacene units in [6]PA and [7]PA[27] are aromatic. This difference could be ascribed to the much larger diradical character of [6]PA and [7]PA compared to [4]PA. Therefore, the lateral extension in [6]PA and [7]PA provides the opportunity to form local aromatic sextets along the central row of the backbone, resulting in different electronic structures.

To further understand the ground-state electronic structure of compound **1**, we conducted magnetic measurements such as variable temperature (VT) NMR, electron spin resonance (ESR) and superconducting quantum interference device (SQUID) measurements. The ^{1}H NMR spectrum of 1 in THF-d_8 at room temperature exhibited one almost flat baseline and cooling of sample to −80 °C also did not obtain full resolution (Supplementary Fig. 3). The NMR broadening can be explained by the thermal population of triplet diradical species at elevated temperatures, as expected for species with strong diradical character. Further experimental evidence was obtained by EPR measurements on **1** in solid and solution. The EPR intensities of compound **1** in powder state and dilute toluene solution decreased with the lowering of temperature (Fig. 5b and Supplementary Fig. 6a), and fitting of the data in both solid state and frozen solution by using Bleaney–Bowers equation[48] gave a singlet-triplet energy gap ($\Delta E_{S\text{-}T}$) of −1.41 kcal/mol and −1.74 kcal/mol, respectively (Fig. 5c and Supplementary Fig. 6b). In the solid states, we could observe the weak axially symmetric triplet state EPR signals corresponding to the $\Delta M_s = \pm 1$ transition (Fig. 5a), and the spectral simulation showed the spin-Hamiltonian parameters of $S = 1$, $g = 2.0022$, $|D/hc| = 0.00825\ cm^{-1}$, and $|E/hc| = 0.00191\ cm^{-1}$. Accordingly, the spin distance was determined to

https://doi.org/10.1038/s41467-024-55556-5

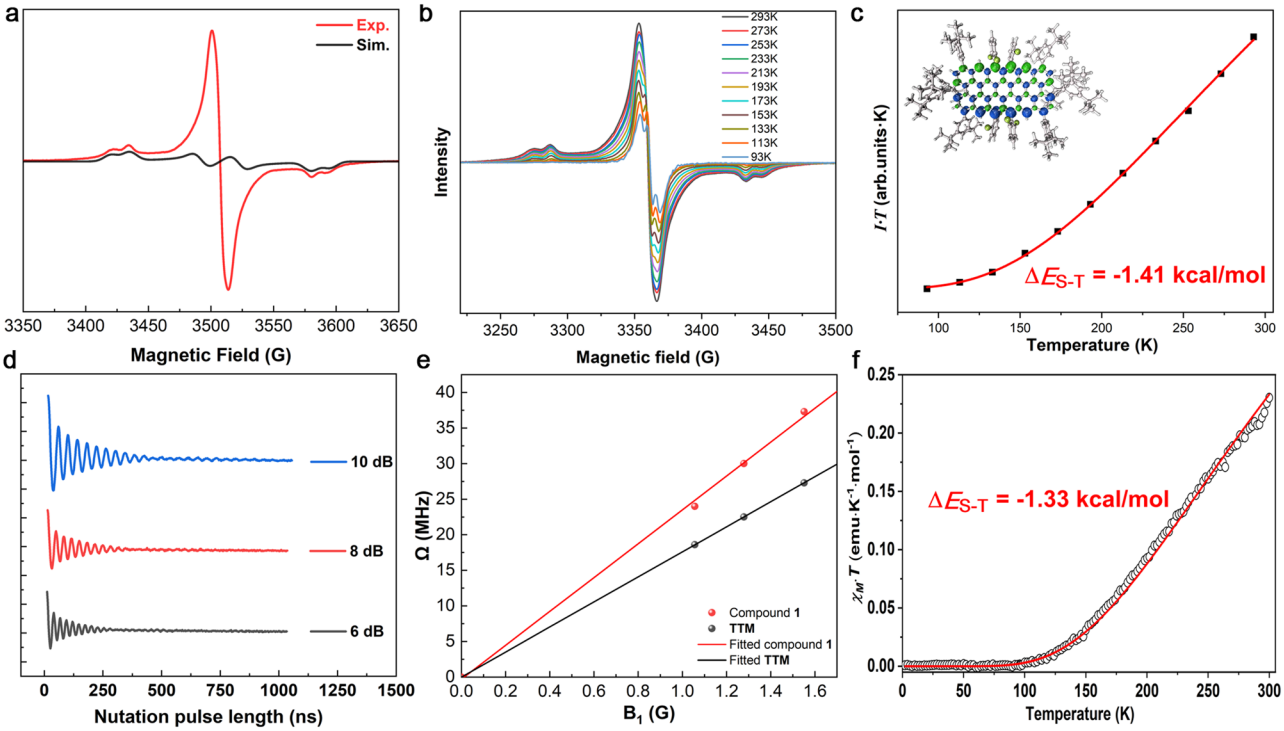

Fig. 5 | Magnetic properties of 1. a X-band cw EPR spectra of compound **1** in toluene at 293 K (red line: experiment; black line: simulation; simulation parameters: $S = 1$, $g = 2.0022$, $|D/hc| = 0.00825\ cm^{-1}$, and $|E/hc| = 0.00191\ cm^{-1}$). **b** Variable-temperature EPR spectra of compound **1** in solid form. **c** fitted $I \times T$-T curve by using Bleaney–Bowers equation. I: EPR intensity, T: temperature in K. Inset is the calculated spin density distribution of the singlet diradical form. **d** Dependence of the Rabi oscillations of **1** on the microwave power attenuation. **e** Corresponding dependence of the Rabi frequency (Ω) on the $\mathbf{B_1}$ field. Key: standard radical TTM (black line; the molecular structure of TTM is shown in Supplementary Fig. 4d), **1** (red line). **f** χ_M T-T plot in the SQUID of measurement of the power **1**, the solid line is the fitting curve according to Bleaney–Bowers equation.

be 6.9 Å, which close to distance of the two zigzag edges of hexacene (7.06 Å) in the crystals. Rabi cycles at 70 K by an echo-detected nutation experiment of compound **1** was conducted (Fig. 5d), and a stable tris(2,4,6-trichlorophenyl)methyl (TTM, $S = 1/2$) radical is employed as an external standard. The results show that the slope of the linear dependence of Rabi frequency on the B_1 magnetic field is approximately $\sqrt{2}$ times that of a doublet species ($S = 1/2$), indicating the triplet species derived by thermal excitation (Fig. 5e)[49,50]. The spin-lattice relaxation time (T_1) and spin coherence time (T_m) of **1** were obtained using the inversion recovery method and Hahn-echo sequences (Supplementary Fig. 4 and Supplementary Fig. 5). The spin-echo decay curves of **1** were fitted with an exponential decay to extract T_1 of 16.7 ms and T_m of 0.85 µs at 70 K. Compared to most reported radicaloids (Supplementary Table 2)[51–55], *peri*-hexacene **1** exhibits a longer spin-lattice relaxation time ($T_1 = 16.7$ ms) and a comparable spin coherence time ($T_m = 0.85$ µs), with T_m significantly exceeding the duration of spin manipulation pulses (on the order of 10 ns) by nearly two orders of magnitude. These characteristics highlight its potential applications in quantum information processing and two-qubit systems[56–60]. Furthermore, we also carried out superconducting quantum interference device (SQUID) measurements for the microcrystalline sample of **1** at 2–300 K. The magnetic susceptibility increased with increasing temperature, and the singlet-triplet energy gap ($\Delta E_{S\text{-}T}$) was estimated to be −1.33 kcal/mol by careful fitting of the data by using the Bleaney–Bowers[48] equation (Fig. 5f), consistent with the above EPR results. All these indicate that compound **1** is an open-shell singlet diradicaloid and exhibits a large diradical character with a small singlet-triplet energy gap. For comparison, the [4]PA derivative (−2.5 kcal/mol)[26] showed a larger $\Delta E_{S\text{-}T}$ value, in consistency with its smaller diradical character. On the other hand, broken-symmetry DFT calculations (UB3LYP/6-31 G(d,p)) also predict that the open-shell singlet biradical state of **1** has lower energy compared to the triplet biradical state, and the singlet-triplet energy gap ($\Delta E_{S\text{-}T}$) is calculated to be −2.08 kcal/mol, which is consistent with the above experimental results. In addition, DFT calculations also gave a triplet-quintet energy gap ($\Delta E_{T\text{-}Q}$) of −21.79 kcal/mol for **1**. This large $\Delta E_{T\text{-}Q}$ value is in accordance with its small tetraradical character.

The UV-vis absorption spectra of **1** was recorded in carbon tetrachloride and compared to that of precursor **8** in DCM, as illustrated in Fig. 6a. Compound **8** exhibits a well-resolved absorption maximum at 632 nm along with a small shoulder band peaking at 580 nm. In contrast, the absorption spectrum of **1** displays a broad band in the near-infrared (NIR) region with a maximum at 789 nm, which is significantly redshifted compared with that of precursor **8**. Moreover, **1** shows a weak absorption band in the NIR region with maximum (λ_{max}) at 1090 nm along with a shoulder (λ_{sh}) at 1197 nm (Fig. 6a). **1** also displays multiple intense absorption bands in the visible region. The NIR absorption band has a similar structure to that in [4]PA derivative[26] and [7]PA derivative[27], however, the intensity is much weaker. Furthermore, the characteristic long-wavelength shoulder peak for **1** is strong indication that it has an open-shell singlet ground state, and the band is originated from the ground-state HOMO,HOMO → LUMO,LUMO double excitation[61]. The optical band gap (E_g^{opt}) of **1** from the onset of its UV/Vis absorption is roughly estimated to be 0.99 eV, which is smaller than that of [4]PA derivative (1.12 eV)[26] due to the π-extension.

The electrochemical property of **1** was investigated by differential pulse voltammetry (DPV) and cyclic voltammetry (CV) measurements in dichloromethane (Fig. 6b). Compound **1** displays two reversible oxidation waves with halfwave potentials $E_{1/2}^{ox}$ at 0.04 V and 0.32 V, and two reversible reduction waves with half-wave potentials $E_{1/2}^{red}$ at −1.03 V and −1.24 V (*vs* Fc/Fc^+). Compared with [4]PA derivative, the neighboring oxidation or reduction waves of **1** show a smaller segregation, which can be explained by the larger π-conjugated backbone that reduces the intramolecular Coulomb charge repulsion. In

https://doi.org/10.1038/s41467-024-55556-5

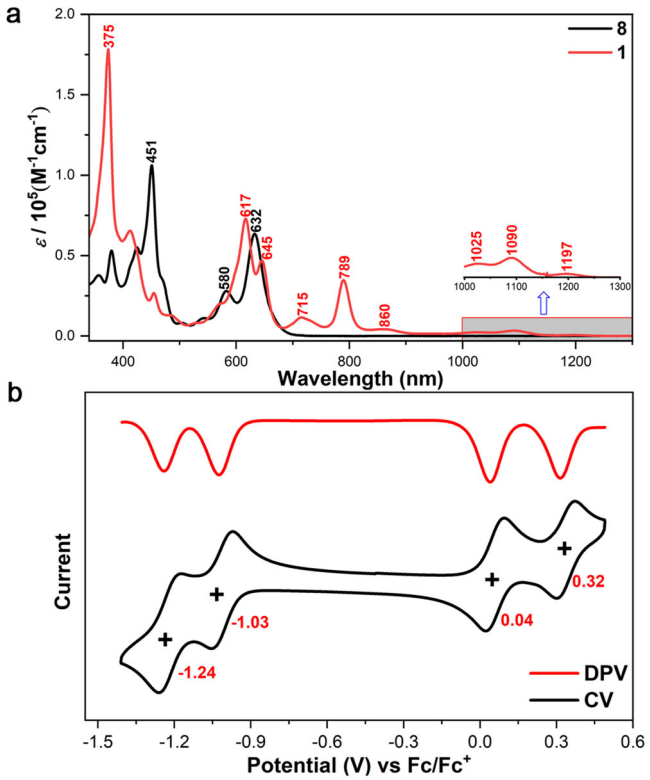

Fig. 6 | Electronic, optic and redox properties of 1. a UV/Vis-NIR absorption spectra of **1** in DCM at room temperature. **b** Cyclic voltammogram and differential pulse voltammogram of **1** in DCM with 0.1 M $Bu_4N{\cdot}PF_6$ as supporting electrolyte; scan rate of 100 mV/s for CV.

addition, according to the onset potentials of the first oxidation/reduction waves, the HOMO and LUMO energy levels of **1** are estimated to be −4.82 eV and −3.76 eV, respectively. Thus, the corresponding electrochemical energy gap (E_g^{EC}) is estimated to be 1.06 eV, which is consistent with the optical energy gap. On the other hand, compound **1** can be chemically oxidized into its corresponding radical cation and dication with $NO{\bullet}SbF_6$ in anhydrous DCM. The radical cation exhibits multiple intense absorption bands in the NIR region with λ_{max} at 858 nm, 1210 nm and 1590 nm, respectively (Supplementary Fig. 2), and a strong EPR signal was observed for the radical cation (Supplementary Fig. 6c). The dication shows an intense absorption band with λ_{max} at 845 nm in the NIR region (Supplementary Fig. 2). All absorption spectra are in agreement with the time-dependent (TD) DFT calculations (Supplementary Figs. 8 to 21).

To reveal the excited-state dynamics of compound **1**, its femtosecond transient absorption (fs-TA) spectra have been recorded in degassed DCM (Fig. 7). As shown in Fig. 7a, upon photoexcitation, two photo-induced bleaching (PIB) bands centered at ~600 and ~644 nm were observed for fs-TA spectra of **1**. The proximity of these two bands to the position of the ground-state absorption peak suggests they are originated from ground-state bleaching (GSB). Furthermore, two excited-state absorption (ESA) bands centered at ~470 and ~520 nm at blue region, as well as a broad band after 660 nm at the red region were observed, which should be originated from its singlet state. With the delay of the time, the TA signal recovered into the ground state without no further spectral evolution, suggesting that no new excited state was formed. From the fitting result of the single-wavelength dynamics of 470 nm (Fig. 7b), we can see that the singlet state decays rapidly into the ground state with a time constant of 26.4 ps. Notably, no triplet state signal was observed in the evolution process of the singlet state, which is consistent with the uphill thermodynamic driving force (1.33 kcal/mol).

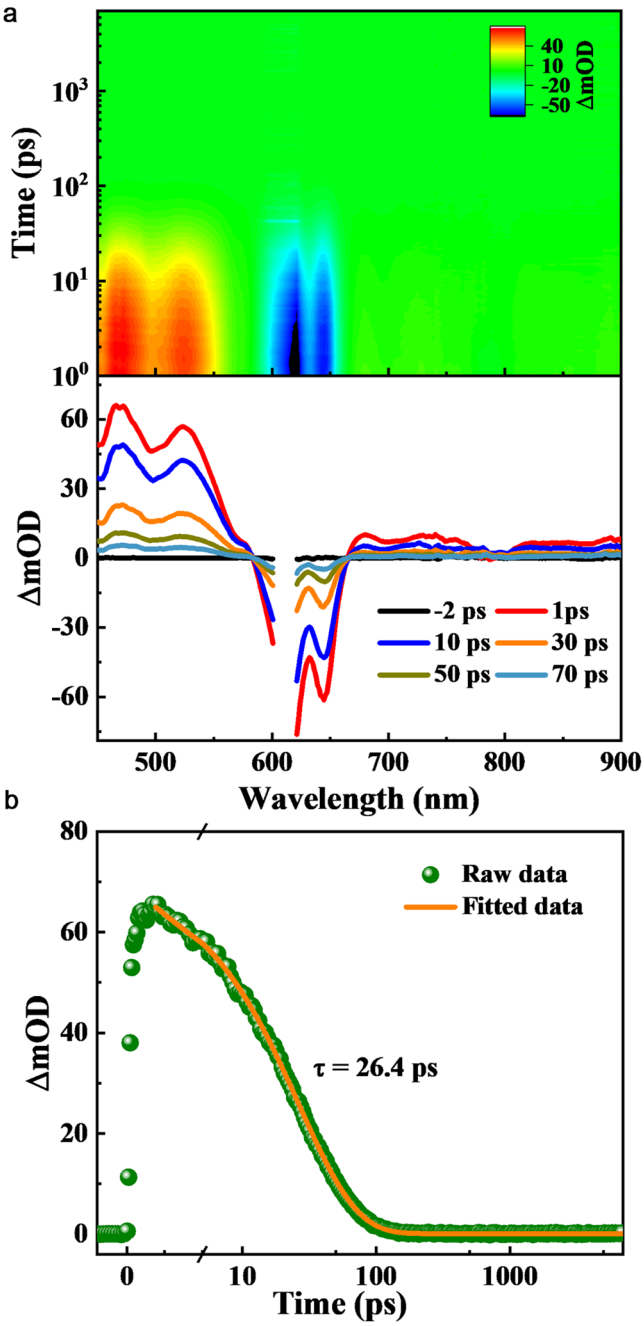

Fig. 7 | Excited state dynamics of 1. a *fs*-TA 2D spectra and time-resolved spectra of compound **1** in degassed DCM (λ_{ex} = 610 nm). **b** Single-wavelength dynamics probed at 470 nm.

Discussion

In summary, a soluble and stable *peri*-hexacene derivative **1** was successfully synthesized and isolated in crystalline form. It exhibits large diradical character and moderate tetra radical character but is still reasonably stable as a result of kinetic blocking of the most reactive sites at the two zigzag edges with the bulky and electron-withdrawing 2,6-dichlorophenyl groups. Analysis shows that it displays a unique electronic structure with five localized aromatic sextets. It exhibits characteristic absorption of singlet open-shell diradicaloids in the NIR region and has a smaller singlet-triplet energy gap. It also shows a global aromatic character that is similar to those of *peri*-tetracene and *peri*-heptacene analogues. Notably, a long spin-lattice relaxation time of 16.7 ms and quantum phase memory time of 0.85 μs was realized in a

1 solution, suggesting its potential application in organic spintronics. On the other hand, it has a small energy gap, showing amphoteric redox behavior and magnetic activity. Our synthetic strategy and physical studies not only reveal the fundamental change of electronic structures and aromaticity of *peri*-acenes upon lateral extension but also provide some insights into the synthesis of larger-size *peri*-acene molecules or other zigzag-edged graphene-like molecules with significant diradical character.

Methods

Synthesis of 1

In a nitrogen-filled glove box, under argon atmosphere and in the dark, a 20 ml vial containing a magnetic stir bar was charged with **8** (50 mg, 0.018 mmol), tert-butoxide potassium (20.4 mg, 0.182 mmol), 18-crown-6 (48.0 mg, 0.182 mmol) and THF (10 mL). The resulting mixture was stirred at room temperature for 6 h, then p-chloranil (11.6 mg, 0.047 mmol) was added. The mixture was kept stirred for 20 min and then the solvent was removed under reduced pressure at room temperature. The resulting residue was purified by flash chromatography (silica gel was neutralized with Et_3N, Hexane/DCM = 3:1) to give **1** (36.5 mg) as a cyan solid in 73% yield. Full experiment details can be found in the Supplementary Information.

Data availability

All data needed to evaluate the conclusions of this study are available in the main text or Supplementary Information. The X-ray crystallographic data for the structures reported in this study have been deposited at the Cambridge Crystallographic Data Centre under deposition numbers CCDC 2337978 (**1**) and 2327038 (**7**). Copies of the data can be obtained free of charge via https://www.ccdc.cam.ac.uk/structures/. Source Data are provided with this manuscript. All data are available from the corresponding author upon request. Source data are provided with this paper.

References

1. Nakada, K., Fujita, M., Dresselhaus, G. & Dresselhaus, M. S. Edge state in graphene ribbons: nanometer size effect and edge shape dependence. *Phys. Rev. B.* **54**, 17954–17961 (1996).
2. Son, Y. W., Cohen, M. L. & Louie, S. G. Half-metallic graphene nanoribbons. *Nature* **444**, 347–349 (2006).
3. Kumar, S. et al. Electronic, transport, magnetic, and optical properties of graphene nanoribbons and their optical sensing applications: a comprehensive review. *Luminescence* **38**, 909–953 (2023).
4. Mousavi, S. T., Badehian, H. A. & Gharbavi, K. Optical spectra of zigzag graphene nanoribbons: a first-principles study. *Phys. Scr.* **97**, 105803 (2022).
5. Wang, Z., Sun, M., Zhao, Y., Xiao, J. & Dai, X. The electronic and transport properties of the folded zigzag graphene nanoribbon. *Surf. Interfaces* **5**, 72–75 (2016).
6. Wang, X. S. et al. Unique magnetic and thermodynamic properties of a zigzag graphene nanoribbon. *Phys. A.* **527**, 121356 (2019).
7. Son, Y. W., Cohen, M. L. & Louie, S. G. Energy gaps in graphene nanoribbons. *Phys. Rev. Lett.* **97**, 216803 (2006).
8. Kan, E. J., Li, Z., Yang, J. & Hou, J. Half-metallicity in edge-modified zigzag graphene nanoribbons. *J. Am. Chem. Soc.* **130**, 4224–4225 (2008).
9. Zhang, D. B. & Wei, S. H. Inhomogeneous strain-induced half-metallicity in bent zigzag graphene nanoribbons. *NPJ Comput. Mater.* **3**, 32–37 (2017).
10. Shao, J., Paulus, B. & Tremblay, J. C. Local current analysis on defective zigzag graphene nanoribbons devices for biosensor material applications. *J. Comput. Chem.* **42**, 1475–1485 (2021).
11. Martín-Martínez, F. J. et al. Inducing aromaticity patterns and tuning the electronic transport of zigzag graphene nanoribbons via edge design. *J. Phys. Chem. C.* **117**, 26371–26384 (2013).
12. Feng, J. et al. How size, edge shape, functional groups and embeddedness influence the electronic structure and partial optical properties of graphene nanoribbons. *Phys. Chem. Chem. Phys.* **23**, 20695–20701 (2021).
13. Li, Z., Huang, B. & Duan, W. The half-metallicity of zigzag graphene nanoribbons with asymmetric edge terminations. *J. Nanosci. Nanotechno.* **10**, 5374–5378 (2010).
14. Clar, E. Polycyclic hydrocarbons. *Angew. Chem. Int. Ed. Engl.* **77**, 875–876 (1964).
15. Clar, E. The aromatic sextet. *Z. f.ür. Chem.* **13**, 200–200 (1972).
16. Clar, E., Zander, M. 378. 1: 12-2: 3-10: 11-Tribenzoperylene. *J. Chem. Soc.*, 1861–1865 https://pubs.rsc.org/en/content/articlelanding/1958/jr/jr9580001861 (1958).
17. Jiang, D. E., Sumpter, B. G. & Dai, S. First principles study of magnetism in nanographenes. *J. Chem. Phys.* **127**, 124703 (2007).
18. Jiang, D. & Dai, S. Circumacenes versus periacenes: HOMO-LUMO gap and transition from nonmagnetic to magnetic ground state with size. *Chem. Phys. Lett.* **466**, 72–75 (2008).
19. Mullinax, J. W. et al. Heterogeneous CPU + GPU algorithm for variational two-electron reduced-density matrix-driven complete active-space self-consistent field theory. *J. Chem. Theory Comput.* **15**, 6164–6178 (2019).
20. Konishi, A., Hirao, Y., Kurata, H. & Kubo, T. Investigating the edge state of graphene nanoribbons by a chemical approach: Synthesis and magnetic properties of zigzag-edged nanographene molecules. *Solid. State Commun.* **175–176**, 62–70 (2013).
21. Ajayakumar, M. R., Ma, J. & Feng, X. π-Extendedperi-acenes: recent progress in synthesis and characterization. *Eur. J. Org. Chem.* **2022**, 01428 (2022).
22. Tombros, N., Jozsa, C., Popinciuc, M., Jonkman, H. T. & van Wees, B. J. Electronic spin transport and spin precession in single graphene layers at room temperature. *Nature* **448**, 571–574 (2007).
23. Biel, B., Triozon, F., Blase, X. & Roche, S. J. N. l. Chemically induced mobility gaps in graphene nanoribbons: a route for upscaling device performances. *Nano. Lett.* **9**, 2725–2729 (2009).
24. Xiao, Y., Ye, Q., Liang, J., Yan, X. & Zhang, Y. Different noncollinear magnetizations on two edges of zigzag graphene nanoribbons. *Chin. Phys. B.* **29**, 127201 (2020).
25. Ajayakumar, M. R. et al. Toward full zigzag-edged nanographenes: peri-tetracene and its corresponding circumanthracene. *J. Am. Chem. Soc.* **140**, 6240–6244 (2018).
26. Ni, Y. et al. A peri-tetracene diradicaloid: synthesis and properties. *Angew. Chem. Int. Ed. Engl.* **57**, 9697–9701 (2018).
27. Ajayakumar, M. R. et al. Persistent peri-heptacene: synthesis and in situ characterization. *Angew. Chem. Int. Ed. Engl.* **60**, 13853–13858 (2021).
28. Rogers, C. et al. Closing the nanographene gap: surface-assisted synthesis of peripentacene from 6,6′-bipentacene precursors. *Angew. Chem. Int. Ed. Engl.* **54**, 15143–14146 (2015).
29. Zhang, X., Li, J., Qu, H., Chi, C. & Wu, J. Fused bispentacenequinone and its unexpected Michael addition. *Org. Lett.* **12**, 3946–3949 (2010).
30. Zophel, L. et al. Toward the peri-pentacene framework. *Chem. Eur. J.* **19**, 17821–17826 (2013).
31. Konishi, A. et al. Synthesis and characterization of teranthene: a singlet biradical polycyclicaromatic hydrocarbon having Kekule´ structures. *J. Am. Chem. Soc.* **132**, 11021–11023 (2010).
32. Kuriakose, F. et al. Design and synthesis of Kekulè and non-Kekulè diradicaloids via the radical periannulation strategy: the power of seven Clar's sextets. *J. Am. Chem. Soc.* **144**, 23448–23464 (2022).
33. Konishi, A. et al. Synthesis and characterization of quarteranthene: elucidating the characteristics of the edge state of graphene nanoribbons at the molecular level. *J. Am. Chem. Soc.* **135**, 1430–1437 (2013).

34. Sun, Z. et al. Dibenzoheptazethrene isomers with different biradical characters: an exercise of Clar's aromatic sextet rule in singlet biradicaloids. *J. Am. Chem. Soc.* **135**, 18229–18236 (2013).
35. Jiang, Q., Tang, H., Peng, Y., Hu, Z. & Zeng, W. Helical polycyclic hydrocarbons with open-shell singlet ground states and ambipolar redox behaviors. *Chem. Sci.* **15**, 10519–10528 (2024).
36. Zeng, W. et al. Rylene ribbons with unusual diradical character. *Chem* **2**, 81–92 (2017).
37. Jiang, Q., Wei, H., Hou, X. & Chi, C. Circumpentacene with open-shell singlet diradical character. *Angew. Chem. Int. Ed.* **62**, 06938 (2023).
38. Shen, J. J. et al. A stable [4,3]peri-acene diradicaloid: synthesis, structure, and electronic properties. *Angew. Chem. Int. Ed.* **60**, 4464–4469 (2020).
39. Doehnert, D. & Koutecky, J. Occupation numbers of natural orbitals as a criterion for biradical character. Different kinds of biradicals. *J. Am. Chem. Soc.* **102**, 1789–1794 (1980).
40. Zeng, W., Qi, Q. & Wu, J. Cyclopenta-fused perylene: a new soluble, stable and functionalizable rylene building block. *Sci. Bull.* **60**, 1266–1271 (2015).
41. Shen, T. et al. Bis-peri-dinaphtho-rylenes: facile synthesis via radical-mediated coupling reactions and their distinctive electronic structures. *Angew. Chem. Int. Ed.* **62**, 11928 (2023).
42. Zou, Y. et al. Peri-pentacene and peri-hexacene diradicaloids. *J. Am. Chem. Soc.* **146**, 27293–27298 (2024).
43. Ostrowski, S. & Dobrowolski, J. C. What does the HOMA index really measure? *RSC Adv.* **4**, 44158–44161 (2014).
44. Chen, Z., Wannere, C. S., Corminboeuf, C., Puchta, R. & Schleyer, Pv. R. Nucleus-independent chemical shifts (NICS) as an aromaticity criterion. *Chem. Rev.* **105**, 3842–3888 (2005).
45. Geuenich, D., Hess, K., Köhler, F. & Herges, R. Anisotropy of the induced current density (ACID), a general method to quantify and visualize electronic delocalization. *Chem. Rev.* **105**, 3758–3772 (2005).
46. Klod, S. & Kleinpeter, E. Ab initio calculation of the anisotropy effect of multiple bonds and the ring current effect of arenes—application in conformational and configurational analysis. *J. Chem. Soc. Perkin Trans.* **2**, 1893–1898 (2001).
47. Lu, T. & Chen, F. Multiwfn: a multifunctional wavefunction analyzer. *J. Comput. Chem.* **33**, 580–592 (2011).
48. Bleaney, B. & Bowers, K. D. Anomalous paramagnetism and exchange interaction in copper acetate. *R. Soc. Lond. Ser. A* **214**, 451–465 (1952).
49. Hu, Z. et al. Endohedral metallofullerene as molecular high spin qubit: diverse Rabi cycles in Gd2@C79N. *J. Am. Chem. Soc.* **140**, 1123–1130 (2018).
50. Sato, K. et al. Polycationic high-spin states of one- and two-dimensional(diarylamino) benzenes, prototypical model units for purelyorganic ferromagnetic metals as studied by pulsed ESR/electron spin transient nutation spectroscopy. *J. Am. Chem. Soc.* **119**, 6607–6613 (1997).
51. Wang, Z. Y. et al. A stable triplet-ground-state conjugated diradical based on a diindenopyrazine skeleton. *Angew. Chem. Int. Ed.* **60**, 4594–4598 (2021).
52. Zhu, Z. et al. Rational design of an air-stable, high-spin diradical with diazapyrene. *Angew. Chem. Int. Ed.* **62**, e202314900 (2023).
53. Komeda, J. et al. Selective transition enhancement in a g-engineered diradical. *Chem. Eur. J.* **30**, e202400420 (2024).
54. Lombardi, F. et al. Quantum units from the topological engineering of molecular graphenoids. *Science* **366**, 1107–1110 (2019).
55. Lombardi, F. et al. Synthetic tuning of the quantum properties of open-shell radicaloids. *Chem* **7**, 1363–1378 (2021).
56. Wolfowicz, G. et al. Author correction: quantum guidelines for solid-state spin defects. *Nat. Rev. Mater.* **6**, 1191–1191 (2021).
57. Graham, M. J., Yu, C. J., Krzyaniak, M. D., Wasielewski, M. R. & Freedman, D. E. Synthetic approach to determine the effect of nuclear spin distance on electronic spin decoherence. *J. Am. Chem. Soc.* **139**, 3196–3201 (2017).
58. Winpenny, R. E. P. Quantum information processing using molecular nanomagnets as qubits. *Angew. Chem. Int. Ed.* **47**, 7992–7994 (2008).
59. Valenta, L. et al. Trimesityltriangulene: a persistent derivative of Clar's hydrocarbon. *Chem. Commun.* **58**, 3019–3022 (2022).
60. Mayländer, M., Thielert, P., Quintes, T., Vargas Jentzsch, A. & Richert, S. Room temperature electron spin coherence in photogenerated molecular spin qubit candidates. *J. Am. Chem. Soc.* **145**, 14064–14069 (2023).
61. Di Motta, S., Negri, F., Fazzi, D., Castiglioni, C. & Canesi, E. V. Biradicaloid and polyenic character of quinoidal oligothiophenes revealed by the presence of a low-lying double-exciton state. *J. Phys. Chem. Lett.* **1**, 3334–3339 (2010).

Acknowledgements

W. Z. acknowledges the financial support from National Natural Science Foundation of China (22175061), Excellent Youth Foundation of Hunan Scientific Committee (2022JJ10025), Key research and development projects of Hunan Province (2022GK2035) and Key research and development projects of Xiangtan City (ZX-ZD20221006). Q. J. thanks the construct program of applied characteristic discipline in Hunan Province, the High-level Talent Program from Hunan University of Science and Engineering and the Science and Technology Innovation Program of Hunan Province (2024RC3224) for financial support. G. L. acknowledges financial support from the National Natural Science Foundation of China (22205117), the Fundamental Research Funds for the Central Universities (63223054, 63233092, 63243139).

Author contributions

J. Z., X-J. F. and W. N. contributed equally to this work. W. Z., Q. J. and B. Z. conceived and designed the experiments. J. Z. and X. F. performed synthetic works, physical characterizations, and computational studies. Y. Y., Y. H., J. S., Y. X. and Z. Z. helped to perform part of synthetic works and physical characterizations. G. L. and W. N. performed the EPR measurements. X-N. F. and H. L. performed the excited-state dynamics study. J. Z., W. Z. and Q. J. wrote the manuscript with input from all authors. All authors contributed to the scientific discussion.

Competing interests

The authors declare no competing interests.

Additional information

Supplementary information The online version contains supplementary material available at https://doi.org/10.1038/s41467-024-55556-5.

Correspondence and requests for materials should be addressed to Baishu Zheng, Qing Jiang, Guangwu Li or Wangdong Zeng.

Peer review information *Nature Communications* thanks Igor Alabugin, who co-reviewed with Michael Commodore and the other, anonymous, reviewer(s) for their contribution to the peer review of this work. A peer review file is available.